Heliyon 10 (2024) e34439

Contents lists available at ScienceDirect

Heliyon

journal homepage: www.cell.com/heliyon

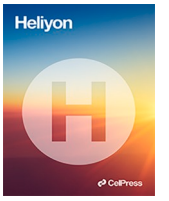

Research article

Ultra-high-sensitive plasmonic sensor based on asymmetric hexagonal nano-ring resonator for cancer detection

Sara Gholinezhad Shafagh, Hassan Kaatuzian *

Photonics Research Lab. (PRL), Electrical Engineering Dept, Amirkabir University of Technology, Tehran, Iran

ARTICLE INFO

Keywords:
Sensitive sensor
Surface plasmon polaritons
Asymmetric nano-ring resonator
Cancer cells
Finite difference time domain method
Sensitivity

ABSTRACT

A highly sensitive sensor based on two metal-insulator-metal waveguides coupled to an asymmetric hexagonal nano-ring resonator detecting cancerous cells is proposed. This novel design is utilized to facilitate the sensing of human cells. The sensing mechanism of the presented optical structure can act as a refractive index measurement in biological, chemical, biomedical diagnosis, and bacteria detection, which leads to achieving high sensitivity in the structure. The main goal is to achieve the highest sensitivity concerning the optimum design. As a result, the sensitivity of the designed topology reaches a maximum value of about 1800 nm/RIU (nm/refractive index unit) by controlling the angle of the resonator. It is evident that the sensitivity parameter is improved, and the reason for the increase in sensitivity is due to the asymmetry of the resonator, which has an 81 % increase in sensitivity compared to the symmetrical resonator, especially for blood cancer cells. The maximum quality factor obtains 131.65 with a FOM of 90.4 (RIU^{-1}). The sensing performance of this proposed structure is numerically investigated using the finite difference time domain (FDTD) method with the perfectly matched layer (PML). Accordingly, the suggested high sensitivity sensor makes this structure a promising therapeutic candidate for sensing applications that can be used in on-chip optical devices to produce highly complex integrated circuits.

1. Introduction

Over the past few years, with the rapid development of optical technology and the rapidly increasing demand for integrated nano-optics devices, light field manipulation is urgently required. Surface plasmon polaritons (SPPs) are electromagnetic excitations propagating along the interface between a metal layer and an insulator. Photonic devices based on SPPs can manipulate and confine light on the subwavelength scale [1]. SPP devices are good candidates for the realization of complex integrated optical circuits such as plasmonic filters [2–6], switches [7,8], modulators [9], couplers [10,11], multiplexers [12,13], demultiplexers [14–16], detectors [17,18], splitters [19], nanolasers [20], amplifiers [21,22], power divider structures [3], solar cells [23], metamaterials [24,25], metasurface structures [26], logical gates [27,28], diodes [29], color filters [30], light scattering [31,32], and slow light devices [33–35]. Furthermore, some novel structures based on hybrid plasmonic photonic crystals have been proposed [36,37].

In recent years, researchers have suggested the optical sensor as a particular type of plasmonic structure due to its outstanding properties for direct sensing processes. SPPs are used in optical devices, specially applications of sensors related to cancer detection. Such optical diagnosis can be implemented in refractive index sensors [38–42]. Applications of such sensors span many fields of biological, chemical, biomedical diagnosis, and bacteria detection, which have been intensively surveyed recently [43,44]. The

* Corresponding author.
E-mail address: hsnkato@aut.ac.ir (H. Kaatuzian).

https://doi.org/10.1016/j.heliyon.2024.e34439
Received 27 April 2024; Received in revised form 21 June 2024; Accepted 9 July 2024
Available online 11 July 2024

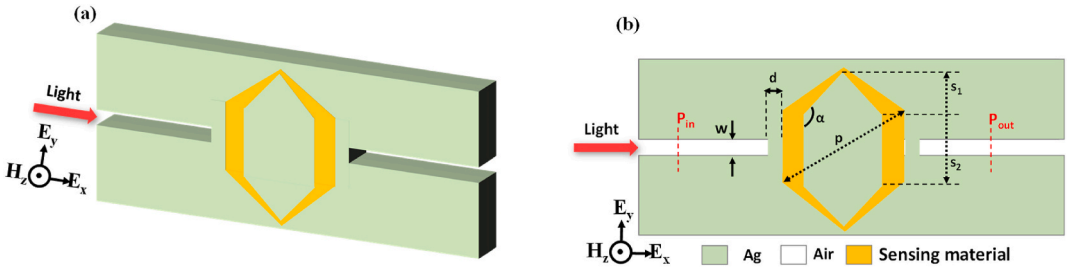

Fig. 1. Structure of AHRR (a) Front view (b) Top view.

working mechanism of the sensor is such that an electromagnetic field by exciting the sensing element produces plasmons that are intensely concentrated on the metal surface. These surface plasmons are highly sensitive to refractive index variations of samples. Other sensing techniques are identified and discussed in Refs. [45–47]. These kinds of sensors can be alternated with other topologies of photonic crystals (PhC) [48–50]. Also, surface plasmon resonance-based sensors are discussed in Refs. [51,52]. Nevertheless, plasmonic devices offer advantages that are capable of subwavelength confinement and usually occupy much less area than PhC devices.

In this present work, a novel metal-insulator-metal topology coupled to an asymmetric hexagonal nano-ring resonator is proposed. This paper aims to determine the refractive index variations of some cancerous cells for early cancer detection. This technique is used to calculate the sensitivity of this sensor. The performance of the designed sensor is such that the sensitivity can be measured via refractive index changes. The capability of the structure is to recognize the six most common cancer types, and it can be seen that blood cancer and breast1 cancer are the most sensitive. The high sensitivity and concern for fabrication conditions are the main goals of the designed structure. Taking all this into account, the highest sensitivity of 1796 nm/RIU (around 1800 nm/RIU) is reached, which is comparable to the reported works. The proposed structure can be fabricated using Electron Beam Lithography (EBL) and chemical etching in such a way that the pattern of silver is deposited on the silicon wafer via the EBL method. Then silver is removed utilizing chemical etching in order to fabricate the waveguides. The current paper is organized as follows: In Sect. 2, a novel structure of the sensor is designed, and a model is explained while it has been discussed about the common cancers in the human body. Next, theoretical analysis is investigated to calculate the transmission spectrum during exposure of the cancer cells in Sect. 3. Also, the sensing performance of the proposed design is investigated by structural parameters considerations in this section. In Sect. 4, the current work is compared with some of the best structures of the reported works. Finally, Sect. 5 is dedicated to the conclusion.

2. Model establishment and theoretical analysis

The schematic diagram of the designed structure is depicted in Fig. 1, which comprises two plasmonic waveguides in a metal-insulator-metal (MIM) structure coupled to a hexagonal nano-ring resonator. Also, a light coupling mechanism between waveguides is discussed and analyzed in a sensor system by Refs. [53,54]. This nano-ring is designed in such a way that the outer part is a regular hexagon (6-gon). In contrast, the inner part is an irregular hexagon with the aim of improving the transmission characteristics and confined propagation. The materials used in the structure include silver and sensing material, which depends on the refractive index (RI). This proposed sensor is used for detecting cancer cells. The structural parameters of the designed sensor are set as: w = 50 nm (the width of two plasmonic waveguides), d = 10 nm (the coupling distance between the exterior hexagon and two waveguides), p = 400 nm (the diameter of the regular hexagon), s_1 = 40 nm and s_2 = 136 nm (the smaller and larger sides of the irregular hexagon). The angle of "α" is 125°. Also, the two smallest angles in the irregular hexagon are 30° and 47°, respectively. The total of the internal angles of the hexagon is 720°, while the irregular hexagon has different angles due to unequal sides. Silver has the lowest power consumption among metals, and its relative permittivity can be characterized by the Drude model as below [55]:

$$\varepsilon(\omega) = \varepsilon_{\infty} - \frac{\omega_p^2}{\omega^2 + i\gamma\omega} \tag{1}$$

Where ε_{∞} is the dielectric constant at the infinite frequency with a value of 3.7, ω_p is the bulk plasma frequency with an energy of 9.1 *ev*, γ is the electron collision frequency with an energy of 0.081 *ev*, and ω shows the angular frequency of incident light in vacuum. It is noteworthy that the imaginary part of the permittivity (the size of loss) is small in the near-infrared range [56]. This structure has been numerically simulated using the two-dimensional finite difference time domain (FDTD) method with perfectly matched layer (PML) absorbing boundary conditions (ABC) in the x-y direction (in-plane direction). The thickness of the proposed structure along the z-direction is considered more extensive than the input wavelength in order to assume 2D-FDTD simplification of an acceptable approximation of 3D-FDTD simulations [57]. As a result, the structure is uniform along the z-direction. In order to obtain the transmittance of the designed structure, two power monitors have been located at the input and output positions. The input and output power are labeled as P_{in} and P_{out}, respectively therefore the transmission characteristics can be found by $T = P_{out}/P_{in}$.

$$T = \frac{P_{out}}{P_{in}} \tag{2}$$

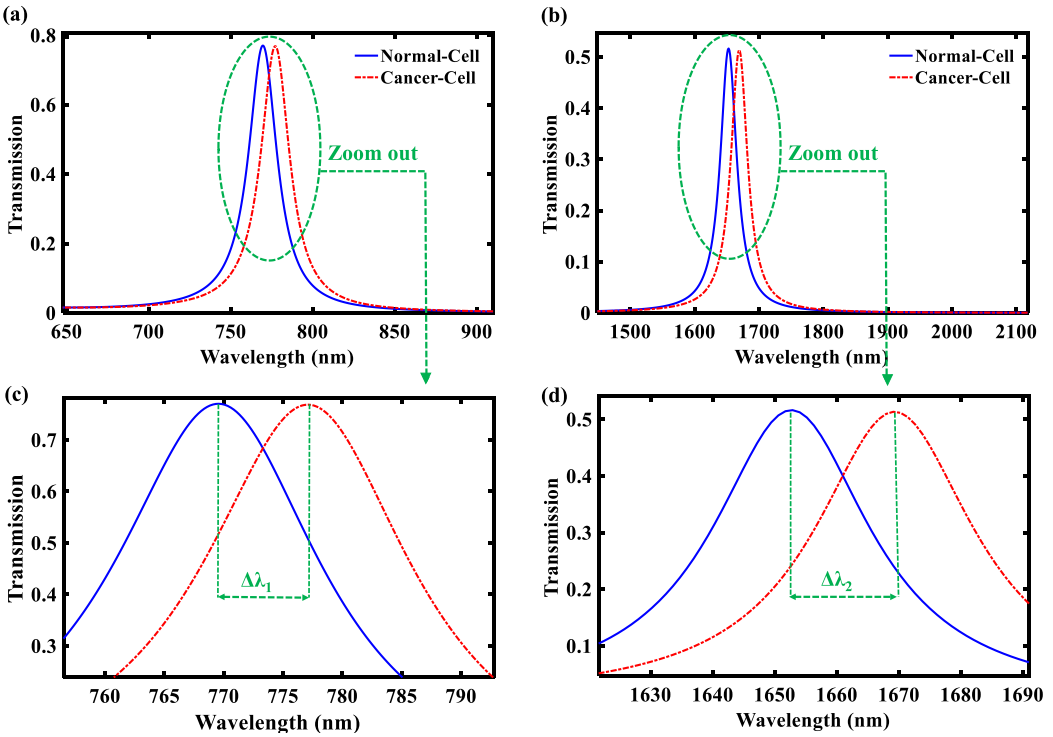

Fig. 2. (a) and (b) Transmission spectrum of the proposed sensor for normal and cancer cells by placing the sample of breast cells. (c) and (d) Zoom-out view of the transmission spectrum at the first and second modes.

In today's life, cancer is one of the deadliest diseases in life. Nowadays, this disease is divided into several common types of cancer, including carcinoma, sarcoma, melanoma, lymphoma, and leukemia [58]. Timely and early diagnosis of cancer is one of the significant challenges, and this challenge is overcome by our designed sensor, which is able to detect refractive index changes in the sensing material. Additionally, the cancerous cell concentration is roughly 80 % in liquid form [59] and the detection is achievable using the measurement approach of this sensor. The most common human cancers occurring worldwide are "Adrenal gland cancer", "Breast cancer", "Blood cancer", "Cervical cancer", and "Skin cancer" [60].

3. Analysis of sensing performance

There are many differences between cancerous cells and normal cells. One of them is the changes in refractive index values, which play a vital role in the prevention, diagnosis, and treatment of human cancer. Our proposed structure shown in Fig. 1 is a suitable candidate for sensing the change in the refractive index of the sample. The device configuration results in a bell-shaped curve at the output power. Its performance is such that light propagation at resonant wavelengths is controlled by the hexagonal nano-ring resonator (HNRR) and the light is reflected to the input port at the non-resonance wavelengths. Therefore, the light can be controlled in this device via the nano-ring resonator coupled to the waveguides, and which possible through irregular hexagons. We employ an FDTD solution of Maxwell's equations to calculate the transmission response of the proposed structure. This operation has been depicted in Fig. 2. It should be noted that the surface plasmon mode is considered in the whole analysis, which propagates along the boundary between insulation and metal. The established model in the MIM waveguide was explained in detail in Ref. [61]. We have adjusted the width of the waveguide (w) to be much smaller than the incident wavelength (λ). Therefore, only the transverse magnetic (TM) mode can propagate in our designed structure. In such a situation, the dispersion relation of this mode can be given by the following equation [61]:

$$\varepsilon_m k_i \tanh\left(\frac{wk_i}{2}\right) + \varepsilon_i k_m = 0 \tag{3}$$

$$k_{m,i}^2 = \beta^2 - \varepsilon_{m,i} k_0^2 \tag{4}$$

Where ε_m and ε_i are the relative permittivity of the metal and insulator, respectively. $k_{m,i}$ are the propagation constants in those mentioned materials, and $k_0 = 2\pi/\lambda$ is the free-space wave vector. The wave vector in the MIM waveguides is also known as β, which is derived from Eq. (4). On the other hand, n_{eff} can be regarded as the effective refractive index of the TM mode in a MIM waveguide and is defined as:

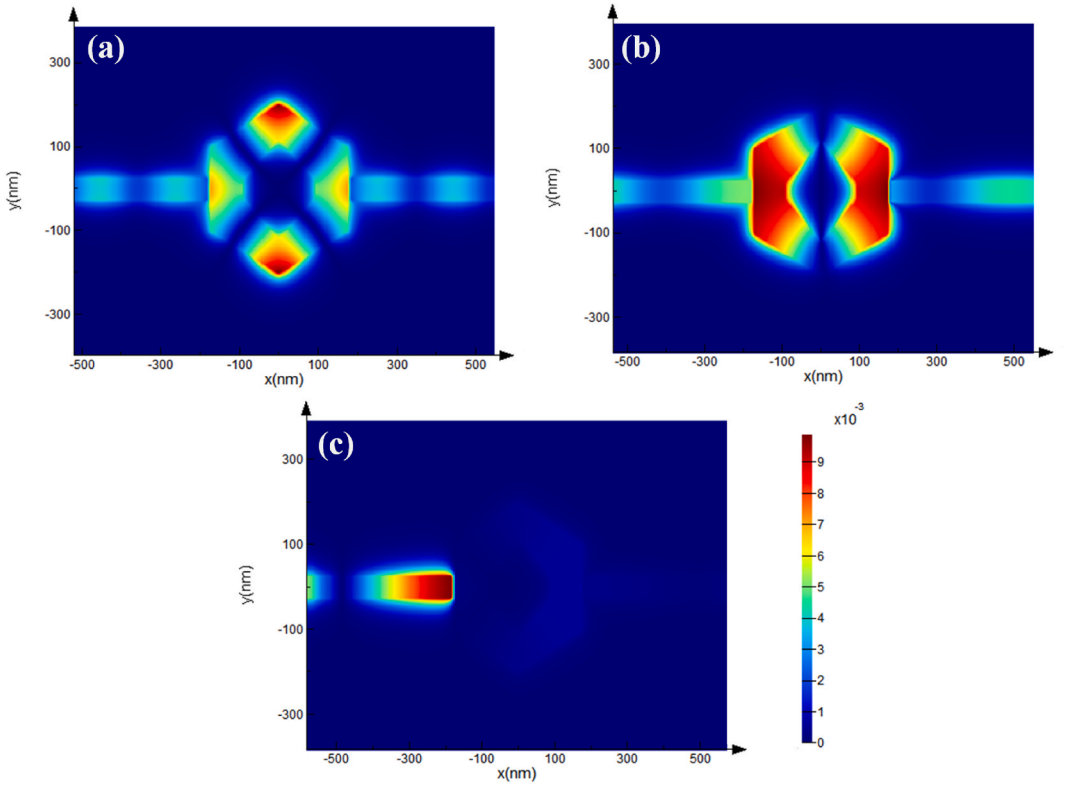

Fig. 3. The absolute parts of the magnetic field component H_z at (a,b) on-resonance ($\lambda_1 = 777$ nm and $\lambda_2 = 1669$ nm) and (c) off-resonance ($\lambda_3 = 1000$ nm) states.

$$n_{eff} = \frac{\beta}{k_0} = \left(\frac{\lambda}{\lambda_{SPP}}\right) + j\left(\frac{\lambda}{4\pi L_{SPP}}\right) \tag{5}$$

Here, n_{eff} represents a complex index of refraction. The real and imaginary parts indicate the guided wavelength in the MIM waveguide (λ_{SPP}) and propagation length (L_{SPP}) of SPPs, respectively. Also, L_{SPP} is determined as the SPP decay length of the energy in the propagation direction and is expressed by Ref. [62]:

$$L_{SPP} = \frac{1}{2Im[\beta]} = \frac{\lambda}{4\pi Im[n_{eff}]} \tag{6}$$

The resonance wavelengths of the transmitted waves in the structure can be achieved by:

$$\lambda = L_{eff}\left(\frac{Re[n_{eff}]}{N - \Phi}\right) \tag{7}$$

Where N represents the mode number and includes natural numbers. Φ is the total phase shift at the corners of the resonator. The effective length of the cavity in our designed structure is called L_{eff}. This length is equal to N λ_{SPP}. The transmission spectrum of our structure has two resonance peaks, which occur at N = 1 for the first resonance peak and N = 2 for the second resonance peak. The effective length of HNRR in the proposed structure can be calculated by:

$$L_{eff} = 2s_2 + 4\sqrt{s_1^2 + \frac{3}{4}s_2^2} \tag{8}$$

As mentioned above, the transmission spectrum of our structure has two resonance modes (N = 1&2) at the wavelengths of 1653 nm and 769.6 nm. The sensing material in the structure is considered for the first case of breast cancer as named breast1 with the basal subtype of "MDA-MB-231" [63]. Breast2 with the subtype of "MCF-7″ is not considered in this study. Fig. 2(a,b) shows the obtained results of the spectrum transmitted signal for normal (healthy) and cancerous cells. The structure exhibits different behavior during exposure to a cancer affected cell compared to a healthy cell. A cancer cell grows uncontrollably migrates to other zones and spreads to other parts of the human body. The main difference is that the cancer cell has more genetic and RI changes compared to a normal cell. The refractive index change is 0.014 from normal to cancer cell for breast1. The refractive indices of normal and cancerous cells are 1.385 and 1.399, respectively, which results in an index difference of 0.014. As shown in Fig. 2(a), the wavelength shifts of the first

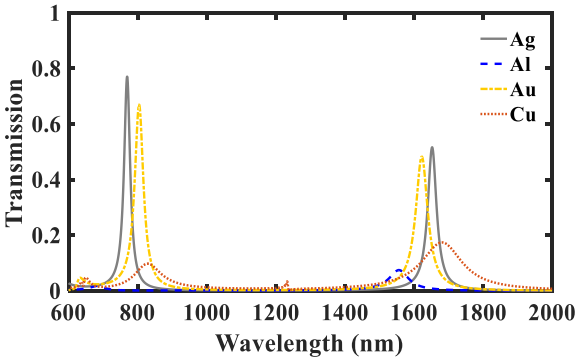

Fig. 4. Transmission spectrum of the proposed sensor for different metals.

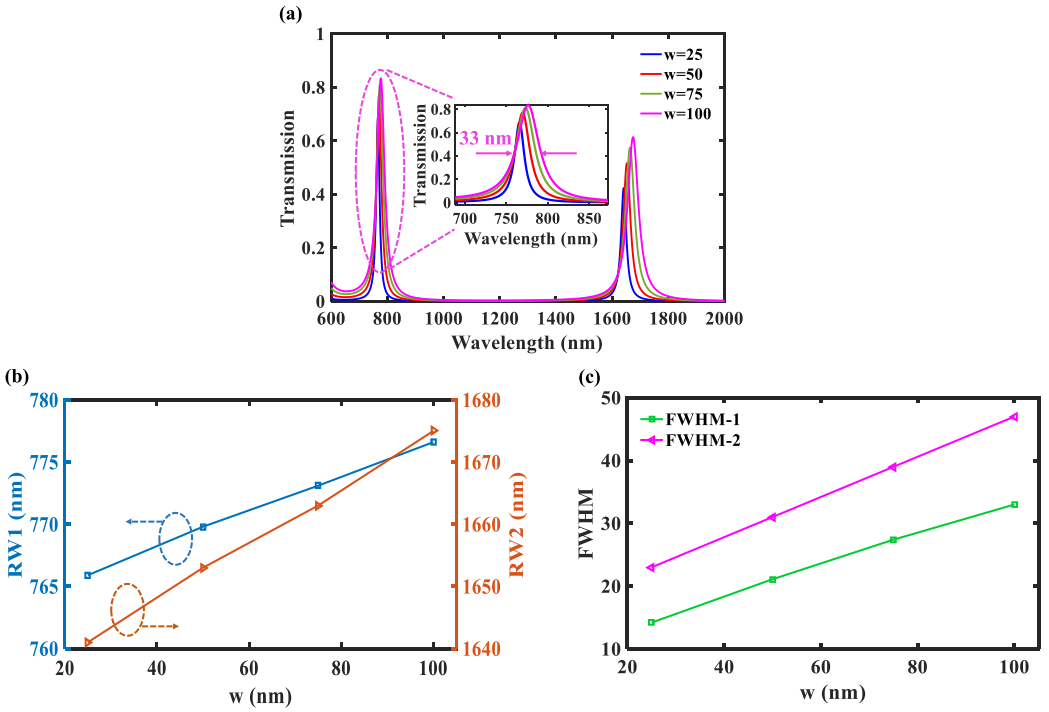

Fig. 5. (a)Transmission spectrum of the designed sensor with different widths of "w" (b) Resonance wavelength of the sensor as a function of "w" (c) A uniform relationship between different values of FWHM and "w" for the first and second modes.

mode towards the right (into the longer wavelengths) will happen in the transmission spectrum during exposure of the cancer cell. In other words, the spectrum experiences the redshift of the resonance wavelengths. The resonance wavelengths of the first mode for normal and cancer cells are 769.6 nm and 777.1 nm, respectively. The same process is repeated for the second mode and leads to a resonance wavelength shift to higher values, as seen in Fig. 2(b). It is seen that the resonance wavelengths of 1653 nm and 1669 nm can be achieved for normal and cancer cells, respectively. For better insight, the zoom-out transmission spectrum of the first and second modes are illustrated in Fig. 2(c) and (d), respectively. The value of L_{eff} is calculated as 769.45 by inserting the indicated values of s_1 and s_2. Since Re[n_{eff}] is obtained 1.99 for the ring resonator filled with the material of normal cells, this results in a resonance wavelength value of about 769.2. As seen, this value confirms the results of FDTD method shown in Fig. 3(a). It is necessary to obtain the resonance wavelength variations ($\Delta\lambda$) for calculating the sensor sensitivity (S), which is defined as the ratio of the wavelength changes to the refractive index variations [64]:

$$S = \frac{\Delta\lambda_N}{\Delta n_c} \quad (\text{nm / RIU}) \tag{9}$$

Where, Δn_c and $\Delta\lambda_N$ represent the differences of refractive indices and resonance wavelength of the normal and cancer cells,

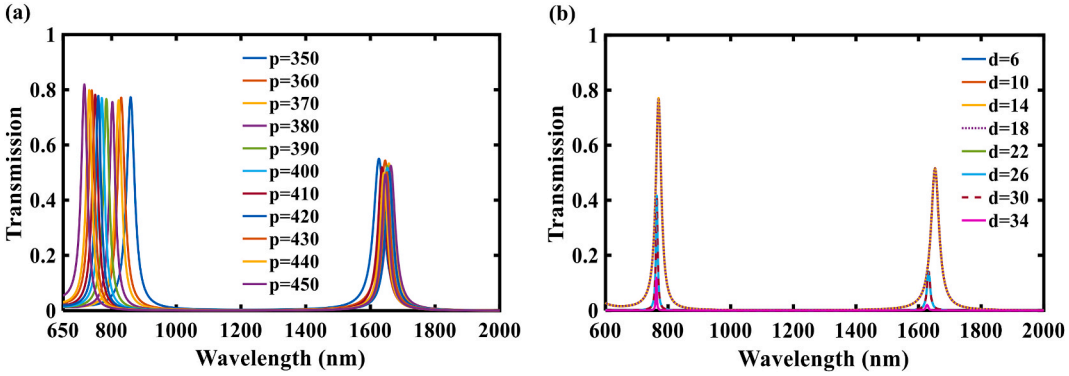

Fig. 6. (a)Transmission spectrum of the designed sensor with different values of "p", and (b) "d".

respectively. In this regard, the sensitivities of our sensor are obtained 736 nm/RIU and 1214 nm/RIU for the first and second mode, respectively, whereas the refractive index variation of breast1 is $\Delta n_c = 0.014$ and the obtained values of $\Delta\lambda_1$ and $\Delta\lambda_2$ are 7.5 nm and 17 nm, respectively. Furthermore, the transmission values at the peak wavelengths of the first and second mode are about 77 % and 52 % which are still acceptable for designing purposes.

To provide a better prospect, the field profile of $|H_z|$ associated with the resonance and non-resonance modes are depicted in Fig. 3. It is noteworthy that the case of human breast cancer cells is investigated in this structure. It can be seen that the most of the light from the source is coupled to the designed cavity known as HNRR and is transferred to the output at on-resonance state. These resonance modes with the highest intensity occur at the wavelengths of $\lambda_1 = 777$ nm and $\lambda_2 = 1669$ nm, which are presented in Fig. 3 (a) and (b), respectively. The wavelength of 1000 nm is considered as an off-resonance state which the energy is not permitted to transfer through the designed sensor. In this way, the light will not be seen at the output of the waveguide.

In addition, the designed sensor is analyzed with different metals to select the best response. In this way, the transmission spectrum of the structure for different metals such as silver (Ag), aluminum (Al), gold (Au), and copper (Cu) is illustrated in Fig. 4. Each metal has its refractive index as a function of the plasmon frequency as well as a unique dielectric response, which is represented by Drude model [65]. As shown in this figure, silver and gold have the best peak transmittance from amongst the metals. Silver has not only the best optical response in terms of transmitted light intensity but also operates at the best suitable wavelength. Based on the results, the peak transmittance values of silver are higher than those of gold, and also silver has a narrower bandwidth of resonance. As a result, we choose silver and consider this metal in our proposed structure due to its lower absorption than gold.

In order to optimize the sensor configuration, we have investigated one of the most essential structural parameters "w", which can act as an influential factor in the transmission spectrum. The influence of various values of "w" on the calculated transmission spectrum by the FDTD method is depicted in Fig. 5(a). In this case, "w" has been changed from 25 nm to 100 nm using 25 nm steps, while other structural parameters are kept fixed. According to this figure, increasing the width provides a higher transmission peak value and a slight resonance wavelength shift. In other words, increasing of "w" causes the redshift of the both resonance modes. Furthermore, a wider FWHM (full width at half maximum) of the spectrum is obtained by increasing "w". Fig. 5(b) presents the effect of this width of "w" on the resonance wavelength of the transmission spectrum. The resonance modes labeled as "RW1" and "RW2" represent the first and second modes, respectively. According to this figure, the resonance wavelengths shift to higher values by increasing the width of "w". As depicted in the figure, as the width is increased, the resonance wavelengths of RW1 and RW2 are increased linearly from 765.9 nm to 776.6 nm and by 1641 nm–1675 nm, respectively. Consequently, the variation of the width affects the RW position and the resonance mode can be tuned through adjusting "w". Fig. 5(c) illustrates a uniform relationship between the width of "w" and FWHM. As shown in this figure, FWHM-1 changes from 14 nm to 33 nm, and FWHM-2 varies from 23 nm to 47 nm for the first and second modes, respectively. The obtained results show that FWHM-1 shifts to higher values and the difference of the two values is 6 nm by a linear increase in "w". Similarly, the shift of each FWHM-2 is about 8 nm for the second mode. Accordingly, a wider bandwidth of the spectrum can be obtained due to the increment of "w". Thus, the sensor's design requires a trade-off between a narrower bandwidth and a higher transmission peak. As a result, "w = 50 nm" can be a suitable choice for sensing performance.

In addition to the structural parameter "w", we have examined two other parameters of the structure such as the coupling distance "d" and the diameter of the regular hexagon "p" and studied the effect of their changes on the transmission spectrum. The effect of different values of "p" from 350 nm to 450 nm is shown in Fig. 6 (a) while we assumed the other parameters to be constant. According to this figure, increasing "p" has a more significant effect on the first mode, and the resonance wavelength of the first mode decreases from 859 nm to 816 nm. Fig. 6 (b) shows the effect of the distance "d" on the performance of the structure. In this case, "d" is increased from 6 nm to 34 nm in a 4 nm step. As can be seen in the figure, the light transmission results are the same in the values of 6–18 nm, but as the "d" value increases, the resonance peak and also the light transmission percentage decrease. Also, the light transmission values are the same between 22 nm and 30 nm. For this reason, we have chosen the optimal value of d = 10 nm.

After choosing the optimal structural parameters in terms of optical performance and efficiency, we survey the best configuration for sensing applications. In this regard, two topologies based on two MIM waveguides coupled to different cavities are investigated. First, the cavity is designed to consist of the asymmetric hexagonal ring resonator (AHRR), and the secondary design of the cavity

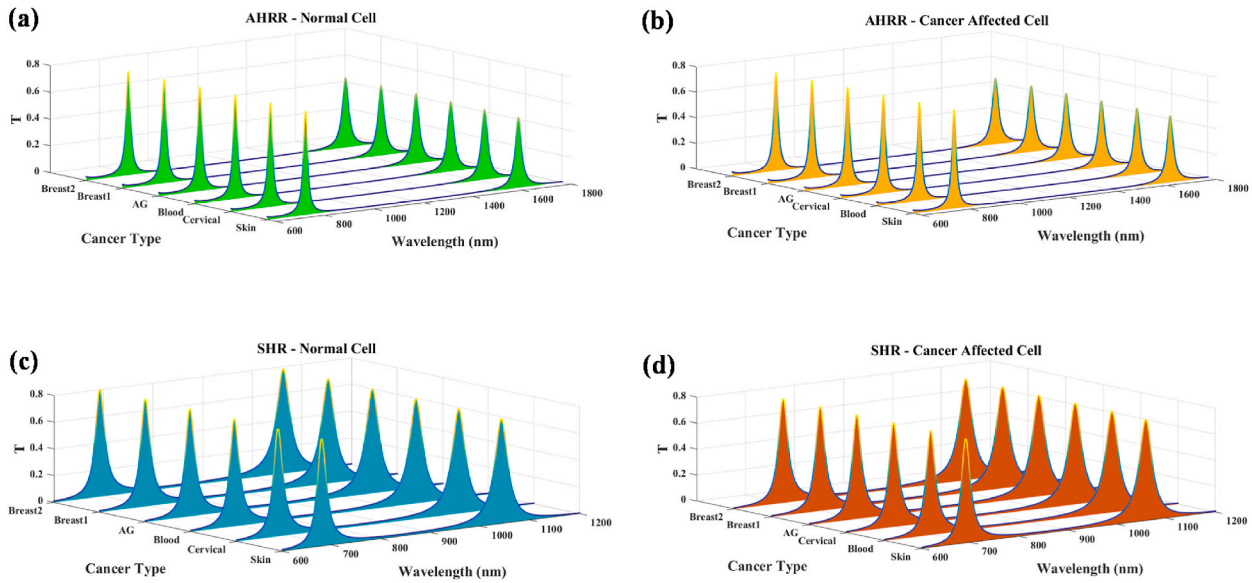

Fig. 7. Transmittance curve of the proposed AHRR for (a) Normal cell and (b) Cancer affected cell. Transmission spectrum of the proposed SHR for (c) Normal cells and (d) Cancer affected cells.

Table 1
The difference in refractive indices of normal cells and cancer affected cells.

Cancer Type	$\Delta\lambda_n$
Skin	0.02 nm
Blood	0.014 nm
Cervical	0.024 nm
Adrenal Gland	0.014 nm
Breast-case-1	0.014 nm
Breast-case-2	0.014 nm

contains a symmetrical hexagonal resonator (SHR). To find out which of these two structures has a better performance in detecting cancer cells, the sensitivity parameters of the symmetrical and asymmetrical cavities of sensors are investigated. Figure (7) shows the transmission spectrum as labeled "T" for two structures of AHRR and SHR using different types of cancer cells. In this study, various normal cells and cancer affected cells in the human body such as skin, blood, cervical, adrenal gland (AG), breast-case-1 (breast1), and breast-case-2 (breast2) are evaluated. The cancer detection depends on the response of the sensor structure to the different refractive indices of the normal cell and cancer affected cell. This difference $(\Delta\lambda_n)$ according to various cancer types is presented in Table 1 in detail [66].

To have a better view of the performance of the two proposed structures, the comparison of the resonance wavelengths of the first and second modes can be observed in Fig. 8. As seen in this figure, the resonance wavelengths of cancer affected cells experience a shift toward higher wavelengths compared to normal cells, both for the first and second modes. Another difference is that the RW of the second mode changes with a slightly gentler slope than the first mode. According to Fig. 8(a), the calculated resonance wavelengths for the first mode related to the proposed structure of AHRR occur at higher wavelengths than the structure of SHR. It means that the structure of SHR operates in the resonance wavelength range of 680–700 nm, while the structure of AHRR works with a steep slope in the 755–780 nm range. Similarly, this issue also applies to the second mode, which corresponds to Fig. 8(b) and(c). As shown, the structure of SHR has a resonance wavelength range of around 1040 nm–1070 nm, and on the other hand, the resonance wavelengths of the structure of AHRR appear in the range of 1620–1670 nm. As can be seen, the bandwidth is increased for the structure of AHRR. As a result, the proposed structure of AHRR is more suitable and provides desirable device performance in terms of operational resonant modes.

As discussed, the difference between normal cell's RI and cancer cell's RI is directly proportional to sensitivity (S). So, Fig. 9 is illustrated for a better understanding of the concept of the mentioned sensitivity. Herein, the sensitivities are calculated for two structures of SHR and AHRR, and on average, the sensitivity of AHRR is higher than SHR for both modes. It is also found that AHRR at the second resonance mode provides better sensitivity values compared to the first resonance modes for all mentioned cancer cells. The lowest sensitivity values of SHR and AHRR for the first mode are 383.33 nm/RIU and 492 nm/RIU, respectively. Accordingly, the lowest sensitivity values for the second mode are obtained as 500 nm/RIU and 1125 nm/RIU for the SHR and AHRR, respectively.

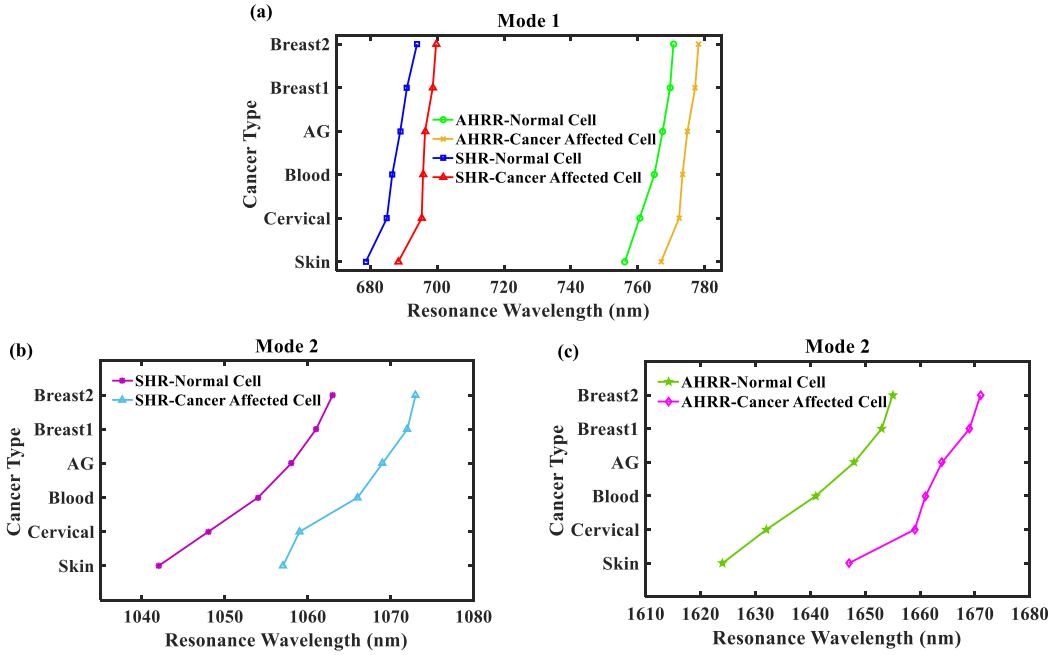

Fig. 8. Comparisons of the RW for the structures of SHR and AHRR between normal cell and cancer affected cells of (a) the first mode (mode-1), (b) and(c) the second mode (mode-2).

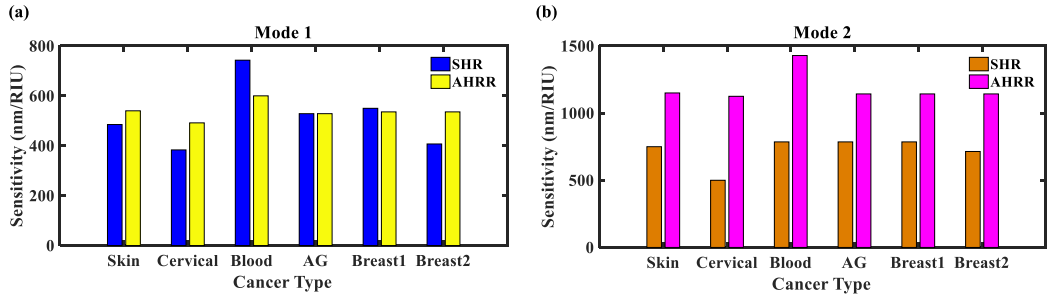

Fig. 9. Sensitivity of the proposed structure of AHRR and SHR for common types of human cancer cells (a) for the first mode, (b) and the second mode.

These lowest values are valid for cervical cancer. It is observed that the highest sensitivities of 742.85 nm/RIU and 600 nm/RIU belong to the SHR and AHRR, respectively, for the first mode. Based on the obtained results, the highest sensitivity values of the second mode are 785.7 nm/RIU and 1428.57 nm/RIU for SHR and AHRR, respectively. Besides, these highest values are obtained for blood cancer. Finally, the designed structures show the least sensitivity to cervical cancer cells, while these structures especially AHRR are more sensitive to the blood cancer cells. Meanwhile, the second resonance mode has a higher sensitivity than the first one. Hence, the structure of AHRR is optimal for both modes, which has a sensitivity higher than 1000 for all human cancer cells. Therefore, it is obvious that the sensitivity parameter is improved in the AHRR with respect to the SHR, and its most remarkable growth of sensitivity is an average of 81 % for the blood cancer cell.

The best parameters to investigate the device's performance are the figure of merit (FOM) and quality factor (QF). FOM is defined as the ratio of the sensitivity to FWHM (FOM=S/FWHM). Also, QF is defined as the ratio of the resonance wavelength of the first or second mode to FWHM (QF = $\lambda_{1,2}$/FWHM) [67]. By optimal the structural parameters and considering the best sensitivity values for breast1 cancer cell, the maximum values of FOM of the first and second resonance modes are obtained equal to 84.38 (RIU^{-1}) and 90.40 (RIU^{-1}), respectively. Furthermore, the QF values of 119.36 and 131.65 are obtained for the first and second modes, respectively.

According to Fig. 9, the results depict that the highest sensitivity values are for blood and breast1 cancer cells, so we examined these two types of cancer cells in the structure of AHRR with different angles of "α" and reached exciting results. Fig. 10 shows the transmission spectrum of the structure of AHRR for different angles considering from "α_1" to "α_6". The angle of "α_1" is considered to be 125°.

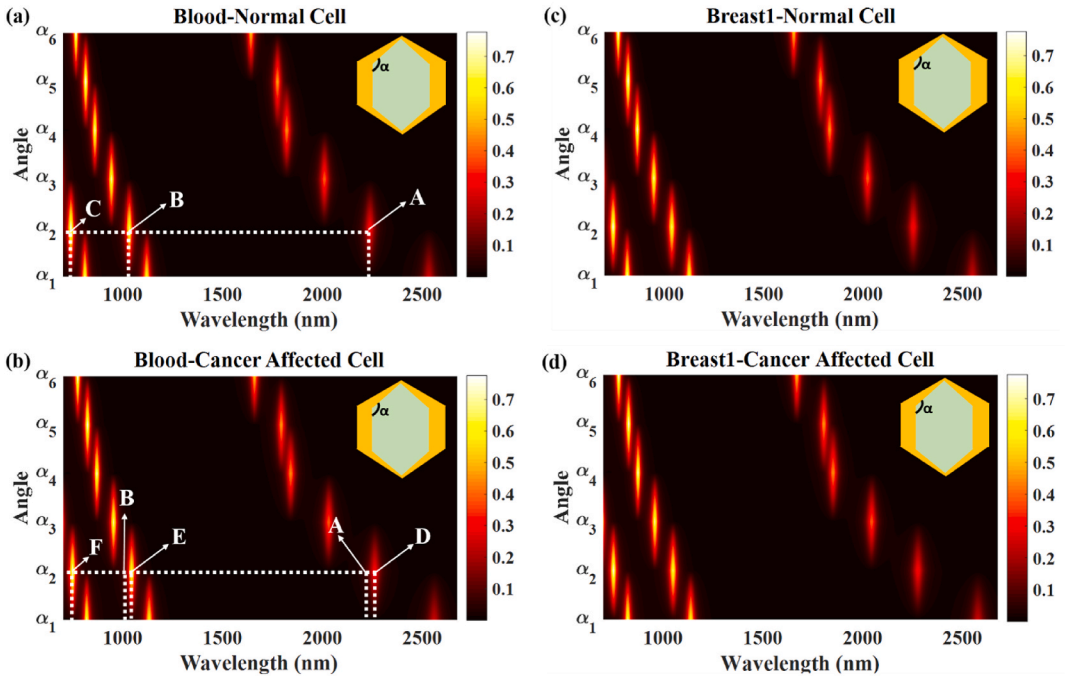

Fig. 10. Transmitted power for the various angles of "α" for (a) blood normal cell, (b) blood cancer affected cell, (c) breast1 normal cell, and (d) breast1 cancer affected cell.

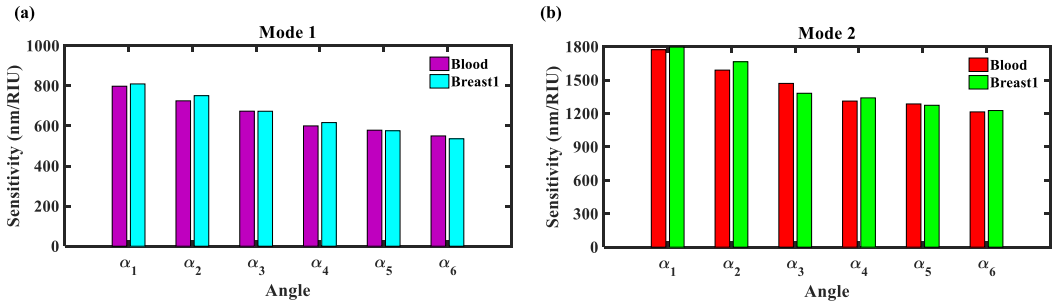

Fig. 11. The calculated sensitivity values for the blood and breast1 cancer cells for (a) the first mode and (b) the second mode.

The change in angles is given by the following equation, which is an arithmetic progression with a common difference of 2 as a constant value with the assumption of "q = 6".

$$\{\alpha_P\}_{P=1}^{q}, \alpha_{P+1} = \alpha_P + 2, P \in \mathbb{N} \tag{10}$$

As shown in Fig. 10, when the angle of "α" is increased from 125° to 129° by a 2° step, the number of the resonance modes of the transmission spectrum of the AHRR is changed from three resonance modes to two resonance modes. In other words, the third mode has disappeared, and only two modes are observed in the transmission spectrum. It can be understood that the resonance wavelengths shift toward higher wavelengths by reducing the angle of "α". Initially, there are two modes, then the third mode occurs at a shorter wavelength for the values of "α_1" and "α_2". All these discussions apply to both normal and cancerous cells. Fig. 10. (a) and (b) represent the transmission spectrum for normal and cancerous blood cells. To investigate the performance of the designed sensor, the sensitivity is calculated. As an example, the maximum transmittance values of the first, second, and third modes for normal cells with the angle of "α_2" occur at the wavelengths of 1032.6 nm, 2238 nm, and 739.37 nm, respectively. These values are specified with the points of "B", "A", and "C", respectively. Similarly, points "E", "D", and "F" show the maximum transmittance values of first to third modes for cancer affected cells. These mentioned points are at the wavelengths of 1042.75 nm, 2260.25 nm, and 746 nm, respectively. It can be observed that the appropriate difference between the two transmission peaks of the second mode of normal and cancer affected cells results in a better sensitivity among the other resonance modes. As a result, the obtained sensitivity values for the first, second, and third resonance modes are 725 nm/RIU, 1589 nm/RIU, and 473 nm/RIU, respectively. Since the sensitivity of the third mode has the lowest values, this resonance mode can be neglected.

Table 2
Comparison of the sensing performance between this work and some other published works.

Reference	Topology	Method	FOM (RIU^{-1})	QF	Max. S (nm/RIU)
[68]	Rectangular resonator	FDTD	17280	–	800
[69]	Ring resonator	FDTD	–	98	868
[70]	A slot resonator and a moving metal nanowall	FDTD	28.2	–	985
[71]	Triangle cavity and an ellipse-ring resonator	FDTD	31.6	–	860
[72]	Rectangular and ring cavities	FEM	75	–	1125
[57]	Si ring resonator	FDTD			636
[73]	Splitting ring cavity and tooth cavity	FEM	122	–	1200
[74]	T-shaped resonator	FDTD	8.68	–	680
[66]	Square lattice of rods in SiO_2	FDTD&PWE	–	25	720
[75]	Split ring resonators	FDTD	24.34	–	1217
[76]	A double circular-hole defect and silicon rods	FDTD&PWE	–	6715	473
[77]	Array of split ring resonators	FEM	258	–	658
[38]	Square ring resonator	FEM	25	27	1367
[78]	Double-ring resonator	FEM	–	–	1070
[79]	Two disk resonators coated with graphene	FDTD	61.55	–	800
[80]	Two double-square resonators	FDTD	143	–	1380
[81]	Ring resonator containing tapered defects	FDTD	159.6	–	1295
[82]	Three parallel rectangular cavity resonators	FEM	14.83	–	1556
[83]	Bowtie cavities	FEM	50	–	1500
[84]	Rectangular resonators and nanorods array	FDTD	20000	93	1090
[85]	Double-ring resonator	FDTD	133	132	1000
[40]	Plasmonic grating-based sensor	FDTD	125	148	1250
[86]	Square ring resonator	FDTD	31.4	–	440
[87]	Nanoring resonator	NA[a]	4300	4310	1700
[37]	A hybrid plasmonic-photonic crystal	FDTD	2388	–	1672
[88]	Periodic array of Au bowtie nanoantennas	FDTD	61	–	612
[89]	Circle-semi-ring coupled resonators	FDTD	66	–	990
[39]	Gold nano-cross array and gold nanofilm	FDTD	98	–	880
[90]	Three resonators and two propagation WGs	FEM	–	–	3885
[67]	Elliptical resonator coupled to a straight WG	FDTD	282	304	550
[91]	H-shaped cavities and WGs	FDTD	108	108	1050
[92]	Plasmonic metasurface (TPM) sensor	FDTD	79	–	1300
[93]	Plasmonic color sensors structure	FDTD	0.24	–	18
[94]	Circular split-ring resonance cavity and WG	FEM	55	–	1114
This work	AHRR	FDTD	90.40	131.65	1796

[a] NA = is not available.

Fig. 11 shows the sensitivity of the proposed sensor for blood and breast1 cells. As mentioned, the highest sensitivity values are obtained at the second resonance mode. Based on the obtained results, by decreasing the values of "α", the sensitivities of the first and second modes for blood cancer cells are increased from 550 nm/RIU to 798 nm/RIU and from 1214 nm/RIU to 1772 nm/RIU, respectively. Similarly, for the breast1 cancer cell, it is found that the sensitivity of the first mode increased from 535 nm/RIU to 809 nm/RIU due to the decrement of angle, while the sensitivities of the second mode obtained as 1226 nm/RIU and 1796 nm/RIU, which is the lowest and highest calculated values. According to the results of "α_1", the highest sensitivities are 1772 nm/RIU for blood cells and 1796 nm/RIU for breast1 cells.

4. Discussions and comparisons

The proposed structure in Fig. 1 is compared with some of the best structures of the reported works in the literature in Table 2. To provide a better prospect, the setups of the different sensors, the topology of the structures, and the entire working wavelength range are compared. It has also been investigated what approach the reported sensors work with, whether they perform based on FDTD or FEM approach. Since we have designed a new sensor structure that includes the asymmetric hexagonal ring resonator (AHRR), the tabular analysis indicates the best performance of this sensor among the other reported sensors. Most of the topologies are derivatives of the ring resonator with MIM setup. The average obtained sensitivity of these reported structures is around 1029 nm/RIU, while the sensitivity of our proposed topology reaches a maximum value of 1796 nm/RIU (approximately 1800 nm/RIU). The results show that our designed topology has better sensing performance and can be a competitive candidate for sensing applications.

5. Conclusions

This paper presents a MIM structure coupled to an asymmetric hexagonal ring resonator for cancer cell detection. The proposed sensor arrangement is used to diagnose the six most common cancer types, with blood and breast1 cancer cells being the most sensitive. An analysis is performed for different cancer types in terms of the transmission response of the sensor. Sensitivity is an imperative part of a sensor's performance which is investigated in our designed structure and the highest sensitivity of 1796 nm/RIU (approximately 1800 nm/RIU) is reached, which is much higher than other reported sensitivities and specificities. The best values of FOM, QF, and S

are the important preconditions for device design. The trade-off between sensitivity, quality factor, and figure of merit is an essential challenge. The proposed sensor ensures high sensitivity with a high FOM of about 90 (RIU-1) to boost the sensing accuracy. The sensor has a maximum QF value of 131.65 which is an acceptable value in such resonator structures. Accordingly, the sensor proposed in this paper provides a new pathway for early cancer cell detection in photonic integrated circuits.

Impact statement

Plasmonic devices are highly desirable which can be made more compact size than photonic crystal ones. Over the past few years, various applications of plasmonic devices have been studied. These structures were designed in different dimensions to affect the motion of the electromagnetic wave. The emission of photons within these structures depends on their wavelength. As a result, some wavelengths of light are allowed to propagate. Plasmonics has become more popular with the reduction of the dimensions by means of surface plasmons. The optical sensor as a particular type of plasmonic structure has been suggested due to its outstanding properties for direct sensing processes.

In this paper, a novel structure has been designed that is used as a sensor. This proposed design has the advantage of an 81 % increase in sensitivity due to the novel geometry scheme. It has several advantages over the previously introduced works. These advantages include high sensitivity, and acting at operating wavelengths for early detection of cancer. Eventually, it can be made in more compact integrated circuits due to the compactness of the design.

CRediT authorship contribution statement

Sara Gholinezhad Shafagh: Writing – original draft, Validation, Software, Methodology, Investigation, Formal analysis, Conceptualization. **Hassan Kaatuzian:** Writing – review & editing, Supervision, Project administration, Conceptualization.

Declaration of competing interest

The authors declare that they have no known competing financial interests or personal relationships that could have appeared to influence the work reported in this paper.

References

[1] W.L. Barnes, A. Dereux, T.W. Ebbesen, Surface plasmon subwavelength optics, Nature 424 (6950) (2003) 824–830.
[2] S.G. Shafagh, H. Kaatuzian, M. Danaie, Design of a plasmonic MIM filter based on ring resonator incorporating circular air holes, in: 2021 29th Iranian Conference on Electrical Engineering (ICEE), IEEE, 2021, pp. 51–55.
[3] N. Korani, A. Abbasi, M. Danaie, Band-pass and band-stop plasmonic filters based on Wilkinson power divider structure, Plasmonics (2023) 1–10.
[4] Y. Qi, et al., Graphene-Enhanced refractive index sensing and narrow-band filtering with crossed bicircular resonator cavity waveguides, Plasmonics (2023) 1–12.
[5] S. Abd-Elsamee, N.F. Areed, H.A. El-Mikati, S.S. Obayya, Tunable multi-channels bandpass InGaAsP plasmonic filter using coupled arrow shape cavities, Photonics 9 (10) (2022) 720. MDPI.
[6] A.N. Taheri, H. Kaatuzian, Numerical investigation of a nano-scale electro-plasmonic switch based on metal-insulator-metal stub filter, Opt. Quant. Electron. 47 (2015) 159–168.
[7] S. Heidari, N. Nozhat, Wideband polarization-independent plasmonic switch based on GST phase-change material, Appl. Opt. 61 (14) (2022) 4068–4073.
[8] M.K. Moazzam, H. Kaatuzian, Design and investigation of N-type metal/insulator/semiconductor/metal structure two-port electro-plasmonic addressed routing switch, Appl. Opt. 54 (20) (2015) 6199–6207.
[9] U. Koch, et al., Ultra-compact terabit plasmonic modulator array, J. Lightwave Technol. 37 (5) (2019) 1484–1491.
[10] A. Dolatabady, N. Granpayeh, Plasmonic directional couplers based on multi-slit waveguides, Plasmonics 12 (3) (2017) 597–604.
[11] A.M.R. Zangeneh, A. Farmani, M.H. Mozaffari, A. Mir, Enhanced sensing of terahertz surface plasmon polaritons in graphene/J-aggregate coupler using FDTD method, Diam. Relat. Mater. 125 (2022) 109005.
[12] M. Mohammadi, M. Soroosh, A. Farmani, S. Ajabi, Engineered FWHM enhancement in plasmonic nanoresonators for multiplexer/demultiplexer in visible and NIR range, Optik 274 (2023) 170583.
[13] S. Bashiri, K. Fasihi, A 2× 1 all-optical multiplexer using Kerr nonlinear nano-plasmonic switch, Opt. Quant. Electron. 51 (11) (2019) 374.
[14] M.R. Rakhshani, M.A. Mansouri-Birjandi, Dual wavelength demultiplexer based on metal–insulator–metal plasmonic circular ring resonators, J. Mod. Opt. 63 (11) (2016) 1078–1086.
[15] A. Azzazi, M.A. Swillam, Nanoscale highly selective plasmonic quad wavelength demultiplexer based on a metal–insulator–metal, Opt Commun. 344 (2015) 106–112.
[16] A. Rostami, A. Bahrami, F. Nazari, H.A. Banaei, Eight-channel wavelength division demultiplexer using multimode interference, in: 2009 Asia Communications and Photonics Conference and Exhibition (ACP), vol. 2009, IEEE, 2009, pp. 1–6.
[17] E. Rastegar Pashaki, H. Kaatuzian, A. Mallah Livani, Hydrodynamic analysis and responsivity improvement of a metal/semiconductor/metal plasmonic detector, Plasmonics 14 (2019) 1639–1648.
[18] E. Khosravian, H.R. Mashayekhi, A. Farmani, Highly polarization-sensitive, broadband, low dark current, high responsivity graphene-based photodetector utilizing a metal nano-grating at telecommunication wavelengths, JOSA B 38 (4) (2021) 1192–1199.
[19] Y. Ye, et al., Design of a novel plasmonic splitter with variable transmissions and selectable channels, IEEE Trans. Nanotechnol. 18 (2019) 617–625.
[20] P. Berini, I. De Leon, Surface plasmon–polariton amplifiers and lasers, Nat. Photonics 6 (1) (2012) 16–24.
[21] A.M. Livani, H. Kaatuzian, Design and simulation of an electrically pumped Schottky-junction-based plasmonic amplifier, Appl. Opt. 54 (9) (2015) 2164–2173.
[22] A.M. Livani, H. Kaatuzian, Modulation–frequency analysis of an electrically pumped plasmonic amplifier, Plasmonics 12 (2017) 27–32.
[23] F. Enrichi, A. Quandt, G.C. Righini, Plasmonic enhanced solar cells: summary of possible strategies and recent results, Renew. Sustain. Energy Rev. 82 (2018) 2433–2439.
[24] M.-R. Nickpay, M. Danaie, A. Shahzadi, Design of a graphene-based multi-band metamaterial perfect absorber in THz frequency region for refractive index sensing, Phys. E Low-dimens. Syst. Nanostruct. 138 (2022) 115114.
[25] B. Ghafari, M. Danaie, M. Afsahi, A multilayered infrared optical absorber based on epsilon-near-zero metamaterials, Plasmonics (2023) 1–8.

[26] A. Hamouleh-Alipour, A. Mir, A. Farmani, Design and analytical evaluation of a high resistance sensitivity bolometer sensor based on plasmonic metasurface structure, IEEE J. Sel. Top. Quant. Electron. 28 (2) (2021) 1–7. Optical Detectors.
[27] S.P.K. Anguluri, S.R. Banda, S.V. Krishna, S. Swarnakar, S. Kumar, The design, analysis, and simulation of an optimized all-optical AND gate using a Y-shaped plasmonic waveguide for high-speed computing devices, J. Comput. Electron. 20 (5) (2021) 1892–1899.
[28] M. Yarahmadi, M.K. Moravvej-Farshi, L. Yousefi, Subwavelength graphene-based plasmonic THz switches and logic gates, IEEE Transactions on Terahertz Science and Technology 5 (5) (2015) 725–731.
[29] Z. Zhu, et al., Enhanced performance of organic light-emitting diodes by integrating quasi-periodic micro-nano structures, Spectrochim. Acta Mol. Biomol. Spectrosc. 292 (2023) 122401.
[30] M. Butt, S. Khonina, N. Kazanskiy, A plasmonic colour filter and refractive index sensor applications based on metal–insulator–metal square μ-ring cavities, Laser Phys. 30 (1) (2019) 016205.
[31] I.L. Rasskazov, A. Moroz, P.S. Carney, Extraordinary fluorescence enhancement in metal-dielectric core–shell nanoparticles, J. Phys. Chem. Lett. 12 (27) (2021) 6425–6430.
[32] S. Sun, I.L. Rasskazov, P.S. Carney, T. Zhang, A. Moroz, Critical role of shell in enhanced fluorescence of metal–dielectric core–shell nanoparticles, J. Phys. Chem. C 124 (24) (2020) 13365–13373.
[33] Z. Vafapour, Slow light modulator using semiconductor metamaterial, Integrated optics: devices, materials, and technologies XXII 10535 (2018) 321–328. SPIE.
[34] M.H. Keleshtery, H. Kaatuzian, A. Mir, A. Zandi, Method proposing a slow light ring resonator structure coupled with a metal–dielectric–metal waveguide system based on plasmonic induced transparency, Appl. Opt. 56 (15) (2017) 4496–4504.
[35] M.H. Keleshtery, A. Mir, H. Kaatuzian, Investigating the characteristics of a double circular ring resonators slow light device based on the plasmonics-induced transparency coupled with metal-dielectric-metal waveguide system, Plasmonics 13 (2018) 1523–1534.
[36] S.G. Shafagh, H. Kaatuzian, M. Danaie, Design and analysis of infrared tunable all-optical filters based on plasmonic hybrid nanostructure using periodic nanohole arrays, Plasmonics (2021) 1–16.
[37] L. Hajshahvaladi, H. Kaatuzian, M. Moghaddasi, M. Danaie, Hybridization of surface plasmons and photonic crystal resonators for high-sensitivity and high-resolution sensing applications, Sci. Rep. 12 (1) (2022) 21292.
[38] M. Butt, S. Khonina, N. Kazanskiy, Plasmonic refractive index sensor based on metal–insulator-metal waveguides with high sensitivity, J. Mod. Opt. 66 (9) (2019) 1038–1043.
[39] H. Chen, et al., Theoretical study of surface plasmonic refractive index sensing based on gold nano-cross array and gold nanofilm, Phys. B Condens. Matter 655 (2023) 414746.
[40] H. Mathuriya, R. Zafar, G. Singh, Plasmonic grating-based refractive index sensor with high sensitivity, IETE J. Res. 69 (6) (2023) 3661–3667.
[41] M. Khorasaninejad, N. Abedzadeh, J. Walia, S. Patchett, S. Saini, Color matrix refractive index sensors using coupled vertical silicon nanowire arrays, Nano Lett. 12 (8) (2012) 4228–4234.
[42] B. Moeinimaleki, H. Kaatuzian, A. Mallah Livani, M. Modabberanbeh, Plasmonic refractive index nano sensor based on triplet coupled stub resonators based Fano resonances, IET Optoelectron. 17 (6) (2023) 257–272.
[43] I.-C. Liu, P.-C. Chen, L.-K. Chau, G.-E. Chang, Optofluidic refractive-index sensors employing bent waveguide structures for low-cost, rapid chemical and biomedical sensing, Opt Express 26 (1) (2018) 273–283.
[44] A.K. Gemta, R. Birhanu, H.D. Mekonnen, U. Sherefedin, K. Woldegiorges, Nanoscale advances, Nanoscale 1 (1) (2018) 1–200.
[45] I. Tathfif, A.A. Yaseer, K.S. Rashid, R.H. Sagor, Metal-insulator-metal waveguide-based optical pressure sensor embedded with arrays of silver nanorods, Opt Express 29 (20) (2021) 32365–32376.
[46] X.-Q. Huang, J.-Y. Su, H.-L. Xu, J.-Y. Zhou, Z.-M. Meng, Highly sensitive gas optical sensing in a multicavity based quasi-parity-time-symmetric structure, Results in Optics 12 (2023) 100446.
[47] S. Sharma, S.K. Mishra, Exploiting the advantages of Ag/ITO/Enzyme trapped gel layers to develop a highly sensitive and selective fiber optic plasmonic urea sensor, Chemosensors 11 (8) (2023) 421.
[48] D. Borges-Silva, C.H.O. Costa, C.G. Bezerra, Robust topological edge states in C 6 photonic crystals, in: Photonics, vol. 10, MDPI, 2023, p. 961, 9.
[49] A.H. Almawgani, S.A. Taya, S.M. AbuIbaid, D.N. Alhamss, I. Colak, Optimization of the temperature dependence of a defect mode in a binary defective photonic crystal, Int. J. Mod. Phys. B 36 (19) (2022) 2250110.
[50] S.A. Taya, M.G. Daher, Properties of defect modes of one-dimensional quaternary defective photonic crystal nanostructure, International Journal of Smart Grid-ijSmartGrid 6 (2) (2022) 30–39.
[51] M. Ghodrati, A. Mir, A. Farmani, Numerical analysis of a surface plasmon resonance based biosensor using molybdenum disulfide, molybdenum trioxide, and MXene for the diagnosis of diabetes, Diam. Relat. Mater. 132 (2023) 109633.
[52] M. Ghodrati, A. Mir, A. Farmani, Proposing of SPR biosensor based on 2D Ti3C2T x MXene for uric acid detection ımmobilized by uricase enzyme, J. Comput. Electron. 22 (1) (2023) 560–569.
[53] M.A. Butt, R. Piramidowicz, Orthogonal mode couplers for plasmonic chip based on metal–insulator–metal waveguide for temperature sensing application, Sci. Rep. 14 (1) (2024) 3474.
[54] M.A. Butt, N. Kazanskiy, S. Khonina, Tapered waveguide mode converters for metal-insulator-metal waveguide plasmonic sensors, Measurement 211 (2023) 112601.
[55] S.G. Shafagh, H. Kaatuzian, M. Danaie, Analysis, design and simulation of MIM plasmonic filters with different geometries for technical parameters improvement, Commun. Theor. Phys. 72 (8) (2020) 085502.
[56] L. Braic, et al., Optimizing strontium ruthenate thin films for near-infrared plasmonic applications, Sci. Rep. 5 (1) (2015) 9118.
[57] M. Danaie, A. Shahzadi, Design of a high-resolution metal–insulator–metal plasmonic refractive index sensor based on a ring-shaped Si resonator, Plasmonics 14 (6) (2019) 1453–1465.
[58] E. Steliarova-Foucher, C. Stiller, B. Lacour, P. Kaatsch, International classification of childhood cancer, Cancer 103 (7) (2005) 1457–1467.
[59] G. Siravegna, S. Marsoni, S. Siena, A. Bardelli, Integrating liquid biopsies into the management of cancer, Nat. Rev. Clin. Oncol. 14 (9) (2017) 531–548.
[60] Z. Deng, et al., DNASE1L3 as a prognostic biomarker associated with immune cell infiltration in cancer, OncoTargets Ther. (2021) 2003–2017.
[61] S.G. Shafagh, H. Kaatuzian, M. Danaie, Ahighly sensitive tunable filter using hybrid 1-D photonic crystal and plasmonic MIM waveguide, Optik 228 (2021) 166174.
[62] J. Tao, B. Hu, X.Y. He, Q.J. Wang, Tunable subwavelength terahertz plasmonic stub waveguide filters, IEEE Trans. Nanotechnol. 12 (6) (2013) 1191–1197.
[63] Y. Li, S. Upadhyay, M. Bhuiyan, F.H. Sarkar, Induction of apoptosis in breast cancer cells MDA-MB-231 by genistein, Oncogene 18 (20) (1999) 3166–3172.
[64] M.-R. Nickpay, M. Danaie, A. Shahzadi, Highly sensitive THz refractive index sensor based on folded split-ring metamaterial graphene resonators, Plasmonics (2021) 1–12.
[65] S.G. Rodrigo, F. García-Vidal, L. Martín-Moreno, Influence of material properties on extraordinary optical transmission through hole arrays, Phys. Rev. B 77 (7) (2008) 075401.
[66] M. Danaie, B. Kiani, Design of a label-free photonic crystal refractive index sensor for biomedical applications, Photon. Nanostruct: Fundam. Appl. 31 (2018) 89–98.
[67] S. Khani, M. Hayati, An ultra-high sensitive plasmonic refractive index sensor using an elliptical resonator and MIM waveguide, Superlattice. Microst. 156 (2021) 106970.
[68] B. Li, et al., High-sensitivity sensing based on plasmon-induced transparency, IEEE Photon. J. 7 (5) (2015) 1–7.
[69] S.-B. Yan, L. Luo, C.-Y. Xue, Z.-D. Zhang, A refractive index sensor based on a metal-insulator-metal waveguide-coupled ring resonator, Sensors 15 (11) (2015) 29183–29191.
[70] F. Chen, D. Yao, Realizing of plasmon Fano resonance with a metal nanowall moving along MIM waveguide, Opt Commun. 369 (2016) 72–78.

[71] A. Akhavan, H. Ghafoorifard, S. Abdolhosseini, H. Habibiyan, Plasmon-induced transparency based on a triangle cavity coupled with an ellipse-ring resonator, Appl. Opt. 56 (34) (2017) 9556–9563.
[72] Y. Tang, et al., Refractive index sensor based on Fano resonances in metal-insulator-metal waveguides coupled with resonators, Sensors 17 (4) (2017) 784.
[73] Y. Zhang, et al., High-sensitivity refractive index sensors based on Fano resonance in the plasmonic system of splitting ring cavity-coupled MIM waveguide with tooth cavity, Appl. Phys. A 125 (2019) 1–5.
[74] L. Wang, Y.-P. Zeng, Z.-Y. Wang, X.-P. Xia, Q.-Q. Liang, A refractive index sensor based on an analogy T shaped metal–insulator–metal waveguide, Optik 172 (2018) 1199–1204.
[75] E. Rafiee, R. Negahdari, F. Emami, Plasmonic multi channel filter based on split ring resonators: application to photothermal therapy, Photon. Nanostruct: Fundam. Appl. 33 (2019) 21–28.
[76] N.A. Mohammed, M.M. Hamed, A.A. Khalaf, A. Alsayyari, S. El-Rabaie, High-sensitivity ultra-quality factor and remarkable compact blood components biomedical sensor based on nanocavity coupled photonic crystal, Results Phys. 14 (2019) 102478.
[77] H.E. Nejad, A. Mir, A. Farmani, Supersensitive and tunable nano-biosensor for cancer detection, IEEE Sensor. J. 19 (13) (2019) 4874–4881.
[78] M.F. Hassan, I. Tathfif, M. Radoan, R.H. Sagor, A concentric double-ring resonator based plasmonic refractive index sensor with glucose sensing capability, in: 2020 IEEE REGION 10 CONFERENCE (TENCON), IEEE, 2020, pp. 91–96.
[79] Y. Shahamat, A. Ghaffarinejad, M. Vahedi, Plasmon induced transparency and refractive index sensing in two nanocavities and double nanodisk resonators, Optik 202 (2020) 163618.
[80] M.R. Rakhshani, Optical refractive index sensor with two plasmonic double-square resonators for simultaneous sensing of human blood groups, Photon. Nanostruct: Fundam. Appl. 39 (2020) 100768.
[81] M. Rahmatiyar, M. Afsahi, M. Danaie, Design of a refractive index plasmonic sensor based on a ring resonator coupled to a MIM waveguide containing tapered defects, Plasmonics 15 (2020) 2169–2176.
[82] R.H. Sagor, M.F. Hassan, S. Sharmin, T.Z. Adry, M.A.R. Emon, Numerical investigation of an optimized plasmonic on-chip refractive index sensor for temperature and blood group detection, Results Phys. 19 (2020) 103611.
[83] Y.-F. Chou Chau, Multiple-mode bowtie cavities for refractive index and glucose sensors working in visible and near-infrared wavelength ranges, Plasmonics 16 (5) (2021) 1633–1644.
[84] M.R. Rakhshani, Refractive index sensor based on dual side-coupled rectangular resonators and nanorods array for medical applications, Opt. Quant. Electron. 53 (5) (2021) 232.
[85] N. Amoosoltani, K. Mehrabi, A. Zarifkar, A. Farmani, N. Yasrebi, Double-ring resonator plasmonic refractive index sensor utilizing dual-band unidirectional reflectionless propagation effect, Plasmonics 16 (2021) 1277–1285.
[86] Y. Sharma, R. Zafar, Plasmonics based refractive index sensor based on square ring resonator, Mater. Today: Proc. 66 (2022) 3698–3701.
[87] Z.E.A. Mohamed, S.A. Taya, A.H. Almawgani, A.T. Hindi, Fano resonance based on coupling between nanoring resonator and MIM waveguide for refractive index sensor, Plasmonics (2023) 1–9.
[88] P. Venugopalan, S. Kumar, Highly sensitive plasmonic sensor with Au bow tie nanoantennas on SiO2 nanopillar arrays, Chemosensors 11 (2) (2023) 121.
[89] X. Jin, J. Li, Y. Ma, Y. Ma, Design of high-sensitive plasmonic sensors with circle-semi-ring coupled resonators, Opt. Quant. Electron. 55 (2) (2023) 104.
[90] D. Qu, Y. Sun, Y. Ren, Q. Wu, C. Li, Research on sensing characteristics of triple independent tuning with high sensitivity based on MIM waveguide, Opt. Quant. Electron. 56 (2) (2024) 137.
[91] S. Khani, M. Hayati, Optical sensing in single-mode filters base on surface plasmon H-shaped cavities, Opt Commun. 505 (2022) 127534.
[92] A.H. Alipour, S. Khani, M. Ashoorirad, R. Baghbani, Trapped multimodal resonance in magnetic field enhancement and sensitive THz plasmon sensor for toxic materials accusation, IEEE Sensor. J. 23 (13) (2023) 14057–14066.
[93] A. Hamooleh-Alipour, A. Mir, A. Farmani, Spectral resolution enhancement of plasmonic color mixing sensor with extremely compact footprint and wide range tuning, Microsyst. Technol. 29 (3) (2023) 301–310.
[94] M. Wang, M. Zhang, Y. Wang, R. Zhao, S. Yan, Fano resonance in an asymmetric MIM waveguide structure and its application in a refractive index nanosensor, Sensors 19 (4) (2019) 791.